RSC Advances

PAPER

View Article Online
View Journal | View Issue

Cite this: *RSC Adv.*, 2026, **16**, 28874

Sustainable earth-abundant bismuth catalytic nanointerfaces using biopolymeric silk fibroin for efficient pollutant reduction

Md. Hasan Ali,[a] Md. Abdur Rahman, *[a] Anwar Ul Hamid [b] and Hasan Ahmad [a]

We unveiled a new route to synthesize catalytic core–shell Bi/SF nanointerfaces using a highly abundant, bioinspired, eco-friendly, low-cost, and multifunctional silk fibroin (SF) scaffold and metallic Bi. SF was first extracted from traditional Rajshahi silk and then dissolved in ethylene glycol using Bi^{3+} ions. Then, Bi/SF nanointerfaces were produced *via* the *in situ* auto-reduction of Bi^{3+} ions and concomitant surface functionalization of metallic Bi with dispersed-SF. Fourier transform infrared, UV-vis, X-ray photoelectron spectroscopy and X-ray diffraction analyses confirmed the successful synthesis of Bi/SF. The multifunctionality and sheeted structure of SF predominantly improved the dispersity, colloidal stability, mesoporosity, spherical shape, and interfacial activity and maintained the rhombohedral structure of the core Bi. Bi/SF nanointerfaces serve as versatile and recyclable catalysts for the sustained reduction of organic pollutants. The catalytic reduction performance was evaluated using four model molecules, namely, Congo red (CR), methyl orange (MO), Eriochrome black-T (EBT) and *p*-nitroaniline (*p*-NA), in the presence of $NaBH_4$. The designed nanointerface competently interacted with electron deficient functionality and exhibited the most efficient reductions against the azo (97.8%, 97.1%, and 83%) and nitro (96.2%) moieties of CR, MO, EBT, and *p*-NA, respectively. These reduction reactions were performed in an aqueous medium at room temperature without any co-catalysts, photoactivation or H_2(g) supply, and were completed within 2–5 min. Time-dependent UV-vis spectra and kinetic studies revealed pseudo-first-order reduction behavior for all substrates, and the rate constants followed the order of EBT > CR > MO > *p*-NA. The recyclability study revealed the sustained activity of the Bi/SF nanointerfaces over five cycles for CR and EBT, maintaining an efficiency above 95%, while MO and *p*-NA showed minor declines. The findings emphasize the synergetic role of the active nanointerfaces in Bi/SF for accelerating redox transformations under mild and sustainable conditions.

Received 15th March 2026
Accepted 12th May 2026

DOI: 10.1039/d6ra02184k

rsc.li/rsc-advances

1. Introduction

Designing catalytic nanointerfaces that combine high activity, structural simplicity, and environmental compatibility remains a central challenge in nanomaterial research.[1,2] Conventional catalysis systems, such as polymer-supported transition metal oxides and mixed-valence ferrites, provide moderate catalytic performance and magnetically retrievable platforms.[3,4] However, these catalysts operate through Fenton-like oxidative pathways for azo dye degradation, producing inorganic sludge and requiring stringent pH control.[4–6] Oxide-based catalysts also exhibit weaker selectivity for the reduction of –N=N– and $–NO_2$ groups under benign conditions, and their synthesis typically demands high temperatures or harsh conditions, which compromises the colloidal stability and interfacial uniformity.[5–8] To achieve practical rates, these systems frequently necessitate high catalyst loadings, photo-induced activation, or co-catalysts. In contrast, carbon-supported metallic interfaces, like activated carbon, graphene, and carbon nanotubes, offer large surface areas and improved electron transport, thereby enhancing the catalytic performance in organic transformations.[9–15] Pd/C and Cu/C remain the benchmarks for nitroaromatic reductions,[9] while Cu/C also demonstrates efficacy in azo-dye reduction. However, these systems suffer from environmental drawbacks, including non-biodegradability, energy-intensive fabrication, and reliance on post-functionalization.[10] Persistent surfactant residues, poor regeneration, and limited compatibility with proteinaceous matrices further detract from their sustainability.[12–14] Moreover, oxygen-sensitive formulations and susceptibility to carbon corrosion or metal leaching during repeated cycles remain critical barriers to sustainable long-term applications.

On the contrary, metallic cores, such as Ni-, Co-, Cu-, Pd-, Ag-, Au-, and Pt-based catalytic interfaces, exhibit size-dependent tunable properties that enable unusual reactivity and

[a]*Polymer Colloids and Nanomaterials Research Lab, Department of Chemistry, Faculty of Science, University of Rajshahi, Rajshahi-6205, Bangladesh*

[b]*Core Research Facilities, King Fahd University of Petroleum and Minerals, 31261 Dhahran, Saudi Arabia. E-mail: arahman@ru.ac.bd*

selectivity.[2,16–20] Compared with carbon-supported metals or metal oxide catalysts, these metallic nanoparticles contain a relatively higher number of active sites per particle, thereby enhancing catalytic application. Particularly, polymer-coated metal-mediated hybrid interfaces address stabilization and sustainability simultaneously.[10,14,21–23] For instance, chitosan-Ag, gelatin-Au, and alginate-Cu systems, in which amine, hydroxyl and carboxylates anchor metal precursors and modulate local polarity, facilitating adsorption and electron transfer.[21–23] Nevertheless, such interfacial designs often require multistep grafting, crosslinking, or ligand exchange, which narrows scalability and introduces heterogeneity at the core–shell boundary. Mechanical resilience and fouling resistance can also be inconsistent, especially under repeated hydride delivery, where polymer segments undergo microstructural changes through hydrolysis under harsh conditions.[20] Furthermore, these catalytic interfaces are not cost-effective, suffer from limited availability, and remain prone to aggregation or undesirable surface poisoning in dispersed media.

To overcome these limitations, attention has increasingly been shifted towards the sustainable catalytic nanointerfaces derived from earth-abundant, biocompatible, and less-toxic components. Accordingly, the rational design of metallic fillers embedded in biopolymer matrices is essential to achieve catalytic efficiency while ensuring sustainability and scalability. Such nanointerfaces can deliver performance comparable to conventional catalysts while simultaneously addressing the shortcomings of oxide, carbon, and noble-metal systems by integrating facile synthesis, interfacial specificity, and operational robustness into a single recyclable platform. The preparation of core–shell catalytic nanointerfaces based on earth-abundant bismuth and biopolymeric silk fibroin (SF) has scarcely been observed in recent studies.[53–56] In this study, Bi^{3+} ions were combined with dissolved silk fibroin (SF) to construct potentially active catalytic nanointerfaces for the reduction of organic pollutant molecules. Bismuth, a post-transition metal with rich redox chemistry and minimal toxicity relative to most noble metals, has emerged as a promising alternative for hydride-mediated reductions.[24–27] Bi nanoparticles efficiently mediate electron transfer from $NaBH_4$ to electrophilic azo and nitro groups, enabling rapid and selective reductions under mild conditions.[28–30] However, bare Bi particles are prone to aggregation, surface passivation, and poor dispersion in aqueous environments, which limit their practical performance and recyclability.[31,32] To address these challenges, a stabilizing milieu is highly required to protect the bare surface of Bi, enhance colloidal stability, and maintain catalytic accessibility.[33–35]

This protective shell not only prevents acidic leaching of metal ions and agglomeration but also enhances pH and substrate-mediated adsorption, facilitates interfacial electron transfer to electrophilic moieties, and accelerates product desorption from reactive sites. Silk fibroin (SF), a naturally abundant protein derived from *Bombyx mori* cocoons, offers a unique solution for designing active catalytic nanointerfaces.[36–39] Its attractive β-sheet structure imparts mechanical stability and flexibility, while peptide side chains offer >NH, $-NH_2$, $-CO_2H$, and –OH functionalities, which enable strong coordination with metal ions and promote adhesion to aromatic substrates.[37,38] Additionally, SF is biomimetic, renewable, biodegradable, structurally versatile, aqueous processable, and capable of forming conformally tunable shells around metal cores without requiring toxic reagents, surfactants, or synthetic grafting.[39–41] These attributes make SF an ideal candidate for constructing robust core–shell architectures. We hypothesize that the tunable structure–function relationship in Bi/SF nanointerfaces enables the faster reduction of azo and nitro pollutants *via* hydride transfer from $NaBH_4$. The catalytic reduction of organic pollutants remains a pressing challenge in environmental chemistry.[7,10,16] Particularly, for sustainable water treatment, conventional methods, such as adsorption, advanced oxidation, and biological degradation, often suffer from incomplete removal, inferior pollutant generation, and slow kinetics.[7,16] In contrast, catalytic reduction using recyclable nanointerfaces offers rapid, selective, and efficient degradation under mild conditions. A core–shell Bi/SF nano-interfacial architecture satisfies these constraints with a mechanistically coherent design, where tuning the Bi : SF mass ratio controls the shell thickness and surface accessibility, thereby optimizing the turnover frequency and recyclability.

The design of sustainable catalytic interfaces from abundant, biocompatible, renewable and relatively low-toxicity metallic components is the central goal of this research. Integrating SF and Bi into a core–shell architecture provides a rational pathway for nanocatalysts that combines structural stability, scalability, recyclability, environmental compatibility, and high catalytic turnover. This study addresses key gaps in catalyst design by uniting facile synthesis, structural simplicity, and high-performance catalysis into a single recyclable platform. The Bi/SF system offers a scalable solution for pollutant remediation, with broad implications for sustainable nanotechnology and environmental chemistry. This modified synthesis protocol eliminates the need for surfactants or high-temperature annealing, while the core–shell design ensures both electron relay and substrate pre-concentration. In this architecture, SF facilitates substrate adsorption and pre-concentration, while Bi mediates rapid electron transfer to electron-deficient moieties, enabling efficient hydride-driven reductions. The synergy between SF and Bi ensures a broad substrate scope, reproducible activity, and recyclability, surpassing the performance of many reported nanointerfaces (Fig. 1).[28–30,39–53] Overall, the designed Bi/SF nanointerfaces minimize the ecological footprint compared to transition and noble-metal systems, offering a cost-effective, sustainable, and environmentally compatible alternative.

Herein, we report core–shell Bi/SF catalytic nanointerfaces that uniquely combine a chemically stable multifunctional SF-shell enriched by nitrogen containing peptide side chains with metallic Bi cores. This architectural design enables rapid hydride-mediated robust reductions at ambient temperatures, outperforming many other catalysts. Complementary experimental characterizations and spectroscopic analyses provide mechanistic details of the electronic and catalytic interactions,

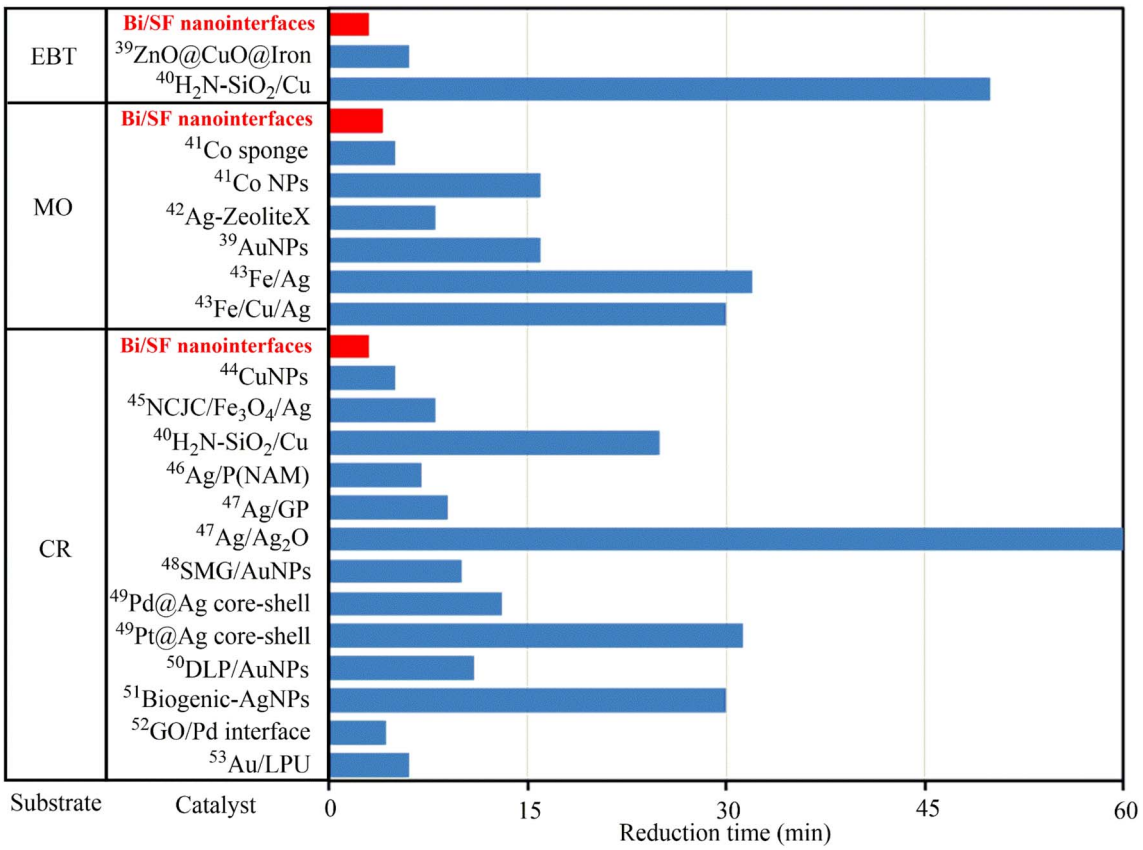

Fig. 1 Summary of the literature on metal oxide- and metal-based catalysts and their efficiency comparison with the Bi/SF nanointerfaces for reducing azo dye compounds.

advancing the development of Bi/SF as an earth-abundant, biocompatible, and sustainable catalytic platform.

2. Experimental section

2.1 Materials

Raw *Bombyx mori* silk cocoons were obtained from the Bangladesh Sericulture Research and Training Institute (Rajshahi, Bangladesh). Bismuth nitrate pentahydrate ($Bi(NO_3)_3 \cdot 5H_2O$) was purchased from Merck Ltd (Mumbai, India). Ethylene glycol (EG) and sodium carbonate were sourced from Loba Chemie Pvt. Ltd (Mumbai, India) and Merck KGaA (Darmstadt, Germany), respectively. Sodium borohydride was procured from Smart Lab (Indonesia). Congo red (CR) and Eriochrome black T (EBT) were purchased from Matheson Coleman & Bell (USA), while methyl orange (MO) was obtained from Merck KGaA (Darmstadt, Germany). *p*-Nitroaniline was supplied by Orgo Chem (Gujarat, India). Sodium hydroxide, hydrochloric acid (37%), ethanol, and other reagents were of analytical grade and used without further purification. Deionized distilled water (DDW) was employed in all experiments.

2.2 Methodology

Silk fibroin (SF) was prepared following the procedure outlined in Scheme 1. Raw *Bombyx mori* silk cocoons were cleaned and stored in the dark until use. The cleaned cocoons were cut into small pieces and subjected to degumming to remove sericin. Specifically, 12.44 g of cut cocoon material was immersed in 0.21% (w/v) aqueous Na_2CO_3 solution and left overnight at room temperature. The swollen cocoons were subsequently

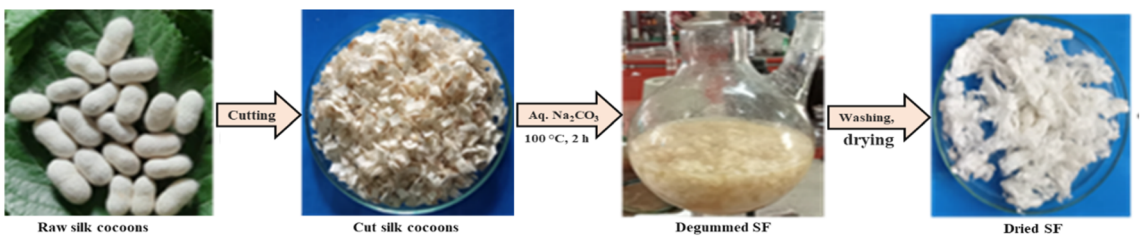

Scheme 1 Production of SF from Rajshahi raw silk cocoons using aqueous Na_2CO_3 at 100 °C.

boiled at 100 °C for 2 h. After boiling, the samples were rinsed several times with DDW to eliminate any residual sericin. Due to the hydrophilic nature of sericin, repeated washing ensured its removal, resulting in brighter SF fibers. The washed SF was squeezed to remove excess water, dried in an electric oven at 50 °C, weighed, and stored in a vacuum desiccator until further use.

2.3 Synthesis of Bi/SF nanointerfaces

Different Bi/SF nanointerfaces were synthesized using a modified facile method.[54] The detailed recipes are presented in Table 1. A three-necked round-bottom flask (RBF) equipped with a reflux condenser, nitrogen gas inlet, and addition funnel was placed on a thermostat magnetic heating stirrer. Bismuth nitrate pentahydrate, $Bi(NO_3)_3 \cdot 5H_2O$ was dissolved in ethylene glycol (EG, 38 mL) under magnetic stirring (500 rpm) at room temperature to obtain a clear solution. The temperature was then raised to 80 °C, and SF (1.45% w/v) was added to an oil bath with continuous stirring (1 h).

The mixture gradually turned light orange (Scheme 2). The dispersion was subsequently transferred into a 50 mL Teflon-lined stainless-steel autoclave, sealed, and heated at 180 °C for 4 h. After natural cooling to room temperature, the reaction mixture formed a black mass. The product was collected by centrifugation (4000 rpm, 5 min), washed twice with ethanol/water (60 : 40 v/v), and rinsed twice with DDW. The resulting particles were dried at 50 °C in an electric oven, collected, and stored in the dark. Reactions with varying concentrations of the metal precursor and SF were performed under identical conditions to evaluate the reproducibility and optimize the nanointerface formation.

2.4 Measurements

The functional groups in the SF and Bi/SF nanointerfaces were analyzed using Fourier transform infrared spectroscopy (FTIR, PerkinElmer FTIR-100, USA) in the range of 4000–200 cm^{-1}. The optical properties were examined using a UV-vis spectrophotometer (Lambda 25, PerkinElmer) over 200–800 nm. The thermal stabilities of the dried bare Bi and Bi/SF nanointerfaces were evaluated using thermogravimetric analysis (TGA, STA 8000, PerkinElmer, Netherlands). The intensity-weighted average hydrodynamic diameters were determined using dynamic light scattering (DLS, NICOMP 380 particle sizer, Santa Barbara, CA, USA). The core–shell nature of the prepared systems was observed using transmission electron microscopy (Philips CM30 and JEOL JEM-2100F, Japan). The surface morphology and particle size distribution were analyzed using scanning electron microscopy (SEM, JSM-6510, JEOL, Japan). The surface elemental composition was determined using X-ray photoelectron spectroscopy (XPS, ESCA-3400, Shimadzu, Kyoto, Japan). The energy-dispersive X-ray (EDX) spectra of the bare Bi nanoparticles and Bi/SF nanointerfaces were recorded using a JEOL JSM-6510A analytical SEM (Tokyo, Japan). X-ray diffraction (XRD) patterns of the bare Bi and Bi/SF nanointerfaces were measured using a Rigaku Ultima IV RINT/D/max-kA diffractometer (Tokyo, Japan) with Cu Kα radiation ($\lambda = 1.54178$ Å) under ambient conditions. Centrifugation for decantation and phase separation was performed using a TG16-WS centrifuge (China). The pH of the dispersions was measured using a Mettler Toledo MP220 pH meter (Switzerland).

Table 1 Recipe to produce different Bi/SF nanointerfaces[a]

Batch no.	Bi^{3+} (g)	SF (g)	EG (mL)	Interfaces
1	1.0984	0.5490	38	Bi/SF (2 : 1)
2	2.1962	0.5473	38	Bi/SF (4 : 1)
3	3.2953	0.5473	38	Bi/SF (6 : 1)
4	1.0984	0	38	Bare Bi (2 : 0)

[a] Conditions: autoclaved at 180 °C and 4 h for Bi/SF; and 200 °C and 6 h for bare Bi.

2.5 Catalytic reduction of the azo and nitro groups

The catalytic activity of the Bi/SF nanointerfaces was evaluated to reduce four model organic compounds: Congo red (CR), methyl orange (MO), Eriochrome black T (EBT), and *p*-nitroaniline (*p*-NA). All reactions were conducted in the presence of the reducing agent, $NaBH_4$. For each reduction study, aqueous solutions of the substrates were prepared in DDW at the desired concentrations. The pH of the reaction mixtures was adjusted using 0.2 M HCl or 0.2 M NaOH solutions. Reduction reactions were conducted in 100 mL reagent bottles fixed on a magnetic stirrer operating at 300 rpm. At room temperature, $NaBH_4$ (0.5 mg) was added to the substrate solution, followed by the introduction of Bi/SF catalytic interfaces (0.2 mg) under continuous stirring. A gradual change in the solution color indicated the progress of catalytic reduction. Aliquots (4 mL) were withdrawn at regular intervals (0.5, 1, 2, 3, and 4 min) and analyzed using a UV-vis spectrophotometer at 200–800 nm to monitor the reaction progress. To optimize reduction conditions and investigate the influence of substrate concentration,

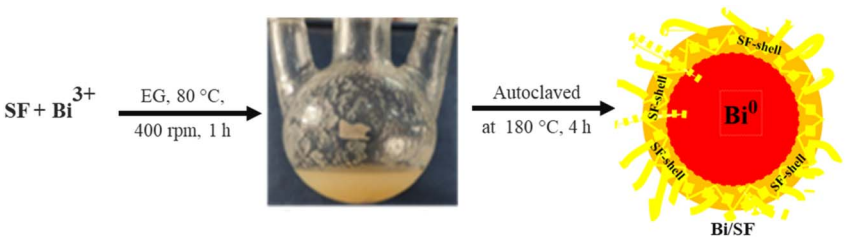

Scheme 2 Production of the Bi/SF nanointerfaces *via* the dissolution of SF and *in situ* auto-reduction of Bi^{3+} ions in EG.

pH, and catalyst contact time, identical procedures were repeated under varied conditions.[55] Therefore, the effects of pH, substrate concentration, and catalyst contact time were systematically investigated for the reduction of azo dyes (CR, MO, and EBT) and *p*-NA. Blank experiments were performed in the absence of Bi/SF nanointerfaces to confirm the catalytic role of the material. Product concentrations in the residual mixtures were quantified using calibration curves constructed from standard solutions. The reduction percentage (R%) was determined with respect to time using a UV-vis spectrophotometer based on eqn (1):

$$R\ (\%) = [(A_0 - A_t)/A_0] \times 100, \quad (1)$$

where A_0 is the initial absorbance of products at λ_{max} and A_t is the absorbance at different intervals of time (t).

Kinetic data of catalytic reductions were fitted with pseudo first-order (eqn (2)) and pseudo second-order equations (Eq. 3):

$$\ln(C_t/C_0) = \ln(A_t/A_0) = -k_1 t, \quad (2)$$

$$1/C_t = 1/C_o + k_2 t, \quad (3)$$

where the pseudo first order rate constant is k_1 (min^{-1}) and the pseudo second-order rate constant is k_2 (L mg^{-1} min^{-1}).

2.6 Recovery, reusability and stability of Bi/SF

After each reduction reaction, the catalyst was recovered from the reaction mixture by centrifugation, washed thoroughly with DDW, and subsequently rinsed with an ethanol–water mixture (7 : 3, v/v) to remove residual reactants and products. The separated nanocatalyst was dried and reused under identical conditions for successive cycles. The reusability of Bi/SF nanointerfaces was evaluated through repeated catalytic cycles. Multiple reduction experiments for all substrates were repeated under similar conditions. The recycled catalyst was collected, dried and characterized using FTIR and PXRD to assess its stability across repeated uses. Measurements were performed in triplicate, and the mean values were reported. Statistical significance was evaluated using a one-way ANOVA. The error bars represent the standard deviation (±5%).

3. Results and discussion

Novel core–shell Bi/SF catalytic nanointerfaces were synthesized from silk fibroin (SF) and *in situ* reduction of earth-abundant Bi^{3+} ions under modified conditions.[54,55] Raw silk cocoons consist of fibroin fiber encased inside sericin. Sericin, a hydrophilic glycoprotein, was removed by mild alkaline hydrolysis from the raw silk cocoon, which yielded 72% SF. Pure SF exhibits amphoteric behavior due to ionizable groups, which dissociate in aqueous medium and enable pH-dependent equilibrium. These functional moieties serve as ligation sites for metal ions, facilitating interface formation.[56] In Bi/SF nanointerface fabrication, SF acts as a ligand, reducing agent, and stabilizer. Bi^{3+} ions strongly coordinate with peptide residues through –SH, –OH, –CONH–, $–CO_2H$, >NH, and $–NH_2$ groups at neutral pH. At 80 °C, Bi^{3+} ions penetrate polypeptide domains, disrupt hydrogen bonding and partially unfold the β-sheet structure. These interactions promote SF dissolution, exposing binding sites for Bi^{3+} adsorption and reduction. Upon thermal treatment at 180 °C, both SF and EG synergistically reduced Bi^{3+} to metallic Bi^0, which nucleated within the reorganized SF matrix. The resulting core–shell architecture featured Bi^0-cores embedded inside SF-sheets *via* strong Bi–O interactions involving phenolate, carboxylate, and amide groups.[54–56] The Bi/SF nanointerface morphology was governed by the Bi : SF weight ratio. Lower Bi loading produced thinner SF shells and smaller Bi cores, enhancing surface accessibility and catalytic turnover. Higher ratios yielded thicker shells, improving colloidal stability and recyclability.[56] These structural variations directly influenced catalytic performance, as demonstrated in subsequent pollutant reduction assays.

3.1 Elemental characterization

The elemental compositions of Bi/SF nanointerfaces and bare Bi were preliminarily evaluated using EDX spectra, as shown in Fig. S1. The wide-scan XPS spectrum of core–shell Bi/SF further confirms the elemental composition, as shown in Fig. 2a. The peaks observed at 158.7 and 164.7 eV are assignable to Bi $4f_{7/2}$ and Bi $4f_{5/2}$, respectively.[54] The C 1s peak at 285.0 eV corresponds to sp^2-hybridized carbon, and oxygenated C-moieties like C–C, C=C and C–O/C=O, originating from the SF-matrix, which is rich in glycine and alanine residues. The N 1s signal, appearing at 400 eV, is attributed to amidic nitrogen (–NHCO–) from the peptide linkage, which confirms the proteinaceous nature of SF-coating. Additionally, two more peaks appeared around 452.5–479.5 eV due to Bi $4d_{5/2}$ and Bi $4d_{3/2}$, further supporting the presence of Bi^0 and minor Bi–O interactions. The O 1 s peak observed at 530.5 eV reflects contributions from Bi–O bonds and carbonyl groups (C=O) in SF, suggesting strong coordination between Bi and SF's oxygenated functional groups. These spectral features collectively validate the dual role of SF as both reducing and stabilizing agents in the synthesis of metallic Bi.

To assess the oxidation states of each element present in the wide-scan spectrum, respective peaks were deconvoluted, as shown in Fig. 2b–f. The deconvoluted C 1 s spectrum of Bi/SF displays four distinct components consistent with the proteinaceous C-environments. A dominant C–C/C–H peak appeared at 284.8 eV, arising from the aliphatic backbone and side-chain carbons. A C–OH and overlapping C–N component was observed at 286.2 eV, attributable to the hydroxyl-bearing residues and peptide-N. In addition, a carbonyl C=O peak was observed at 287.6 eV, corresponding to the amide and other carbonyl functionalities within the SF-matrix. The O–C=O signal, which appears at 289 eV, indicates carboxylate/ester groups, collectively confirming the presence of SF-derived functionalities on the surface of metallic Bi, and the integrity of the protein coating.[56,57] The deconvoluted O 1s spectrum also comprises four chemically distinct components that collectively substantiate the coexistence of SF-derived oxygen functionalities and a very minute oxidized-Bi surface layer. For instance,

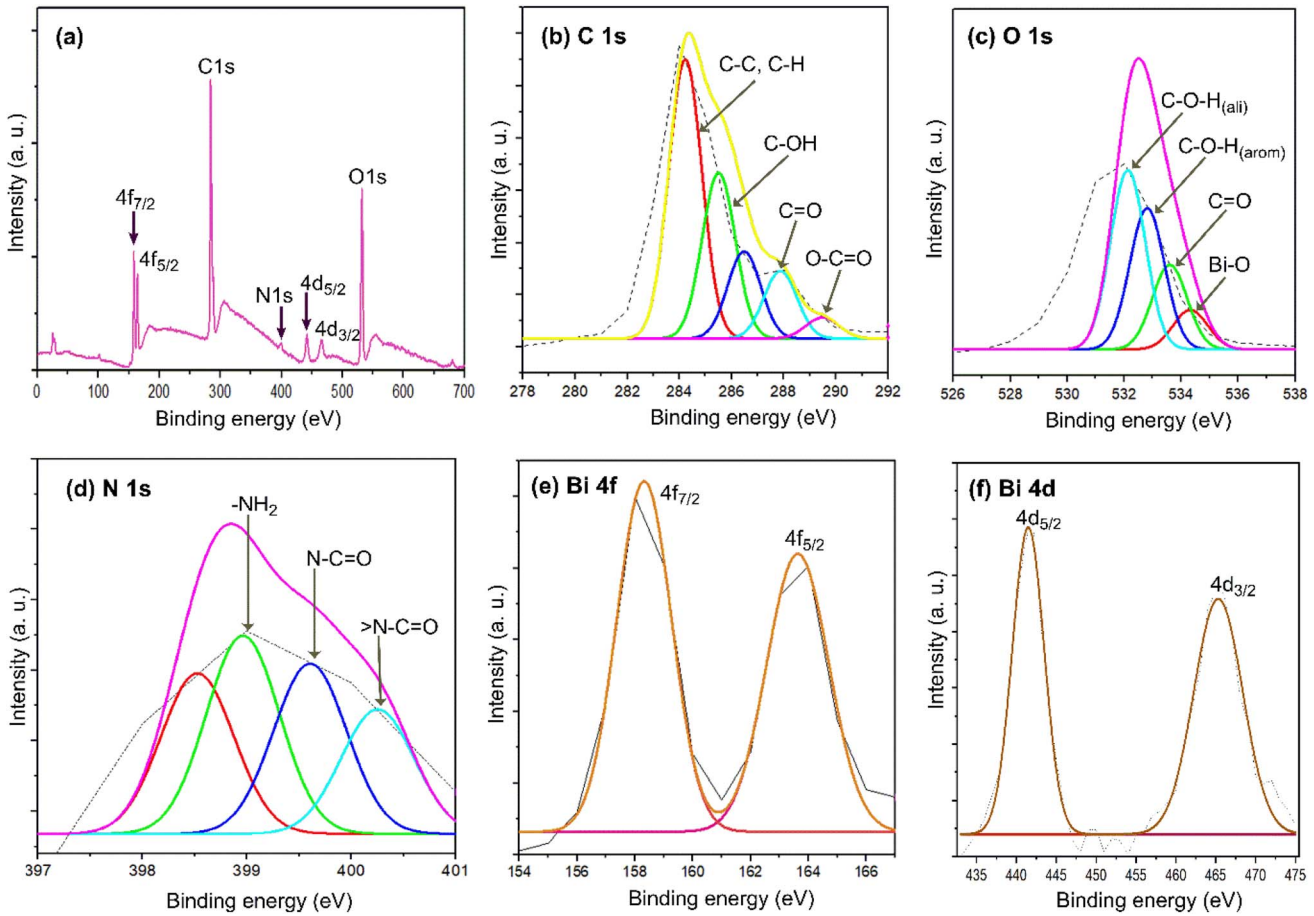

Fig. 2 XPS survey spectrum of the core–shell Bi/SF nanointerfaces (a). Deconvoluted high-resolution core-line XPS spectra of C 1 s (b), O 1 s (c), N 1 s (d), Bi 4f (e) and Bi 4d (f) in the core–shell Bi/SF nanointerfaces.

a Bi–O peak centered at 530.5 eV indicates that surface bismuth oxide species formed upon ambient exposure. A carbonyl C═O component occurred at 531.2 eV assigned to amide groups within the peptide backbones. An aromatic C–O–H contribution was observed at 531.8 eV, consistent with the oxygen bound to aromatic environments, most likely tyrosine side chains or conjugated peptide environments. A C–O–H (aliphatic) feature appeared at 532.5 eV, arising from hydroxyl-bearing aliphatic residues and ether-like oxygen present in the SF-matrix. The deconvoluted N 1 s spectrum shown in Fig. 2d exhibits multiple components consistent with the peptide-rich chemistry of SF. A significant –NH_2 peak centered at 399 eV is attributed to neutral amine termini and side-chain amines. The N–C═O component peak appeared at 399.5 eV, which was assigned to amide nitrogen in the –NHCO– backbone, and >N–C═O also featured at 400 eV, corresponding to more electron-withdrawing or tertiary/condensed amide environments within the SF-matrix. In addition, minor higher-binding-energy contributions, like 400.5–401.5 eV, arise from protonated ammonium species (-NH_3^+) or hydrogen-bond-strengthened amidic-nitrogen. These reflect the local environment and interfacial interactions with the Bi surface. All these components corroborate an intact SF-coating with a predominant amide character and limited terminal/side-chain amines.

The deconvoluted Bi 4f XPS spectrum shown in Fig. 2e displays two characteristic spin–orbit splitting components of elemental Bi. The Bi $4f_{7/2}$ peak is observed at 158.0 eV, and the Bi $4f_{5/2}$ peak is observed at 164.0 eV, with a clear energy separation of 6.0 eV, confirming the presence of Bi^0 as the dominant surface species.[54,56] These binding energies are consistent with reported values for metallic bismuth and indicate successful reduction of Bi^{3+} precursors during synthesis.[56] The absence of any significant higher-energy shoulders or satellite features in these two peaks suggests minimal surface oxidation. However, minor Bi–O contributions cannot be excluded due to the functional ligation of SF and ambient exposures. The sharpness and symmetry of the peaks further support a well-defined metallic state stabilized by the SF-matrix. The deconvoluted Bi 4d XPS spectrum also exhibits two well-resolved spin–orbit components. The Bi $4d_{5/2}$ peak is centered at 440 eV, while the Bi $4d_{3/2}$ peak is observed at 465 eV. The clear energy separation between these two peaks is about 25 eV, consistent with the electronic structure of elemental-Bi (Bi^0).[47,56] The absence of any significant peak broadening or satellite features suggests minimal surface oxidation although minor Bi–O contributions may be present but remain below the detection threshold in this region. The sharpness and symmetry of the Bi 4d doublet further support the stabilization of the metallic Bi phase by the SF-

matrix. All these findings confirm the presence of metallic Bi as the dominant chemical state, in agreement with standard reference values for Bi^0 and corroborating the successful reduction of Bi^{3+} ions during synthesis.

3.2 Functional characterization

Fig. 3 shows the FTIR spectra of (a) bare Bi, (b) SF, (c) Bi/SF nanointerfaces with different ratios of (d) 4 : 1, (e) 6 : 1, and (f) 2 : 1 of Bi and SF. In the FTIR spectrum of bare Bi (Fig. 3a), a broad band appeared at 3400 cm^{-1}, which is assignable to the O–H stretching vibrations originating from physically adsorbed water on the surface of Bi.[24,54] The medium intensity band at 1445 cm^{-1} is attributed to the deformation vibrations of the C–H bonds. For the ionized carboxyl group of oxalate ions, the asymmetric and symmetric stretching bands are expected to occur at 1561 and 1339 cm^{-1}, respectively. Oxalate ions are generated during the solvothermal reduction of Bi^{3+} ions *via* oxidation of EG in the presence of nitro groups at elevated temperature (200 °C). The Bi–O bonds in Bi-oxides vary in length due to geometric structure variations that led to different stretching and deformation vibrations at 400–600 cm^{-1}.[15,30] A broad signal appeared at 554 cm^{-1} assignable to Bi–O vibrations due to ligations of $-CO_2^-$ and O–H groups of oxalates and EG to the surface of metallic Bi.[30,54] The conformational structure of SF can be characterized by absorption bands of amide I. β-sheet structures are represented by the absorption band range of 1616–1637 cm^{-1}. Again, adsorption bands in the ranges of 1638–1655 cm^{-1} and 1655–1663 cm^{-1} were seen that are related to the random-coil and α-helices, respectively. The bands appeared in the range of 1663–1695 cm^{-1} are assignable to the turn's turnery structure of SF.[33,38] In the spectrum of SF (Fig. 3b), a strong band appeared at 3434 cm^{-1} due to O–H stretching vibrations, and the vibration bands at 1641 cm^{-1} and 1563 cm^{-1} correspond to C=O stretching of amide I and secondary N–H bending of amide II, respectively. The characteristic vibration band at 1229 cm^{-1} is related to the C–N and N–H functionalities of amide III, and a medium absorption band is obtained at 1415 cm^{-1} from O–H bending vibration.[33] Furthermore, an absorption peak obtained at 1019 cm^{-1} represents the C–C stretching signal of the glycine–glycine linkage (Silk II). In contrast, in the FTIR spectrum of Bi/SF (Fig. 2c), an N–H bending vibration band (amide II) at 1563 cm^{-1}, and a C–H bending vibration band at 1415 cm^{-1} were clearly visible due to the interactions of SF with Bi. The symmetric stretching band for the ionized carboxyl group appeared at 1339 cm^{-1}, while the Bi remained unchanged. Moreover, Bi/SF showed that the higher intensity of the C=O stretching vibration band (amide I) slightly shifted from 1641.31 cm^{-1} to 1631 cm^{-1}, while the deformation vibrations for the C–H bond appeared at 1445 cm^{-1}. However, the vibration band at 1229 cm^{-1} of amide III disappeared due to the strong ligation of C–O moieties to the metallic Bi surface and hydrogen bonding of the N–H bond. A characteristic signal appeared at 515 cm^{-1} for the Bi–O bond, which shifted from 554 cm^{-1} in Bi/SF nanointerfaces. Significantly, in all the spectra of Bi/SF (b–e), a broad band in the range of 3100–3600 cm^{-1} corresponds to overlapping O–H and N–H stretching vibrations, indicating hydroxyl, amine and amide groups in SF peptide. The C–H stretching modes are observed at 2850–2960 cm^{-1}, arising from aliphatic side chains of fibroin residues. The amide I band, centered around 1620–1650 cm^{-1}, is assignable to C=O stretching vibrations of peptide linkages and reflects the β-sheet or random coil conformations of SF. The precise position varies slightly with the Bi : SF ratio, suggesting conformational adjustments upon nanoparticle

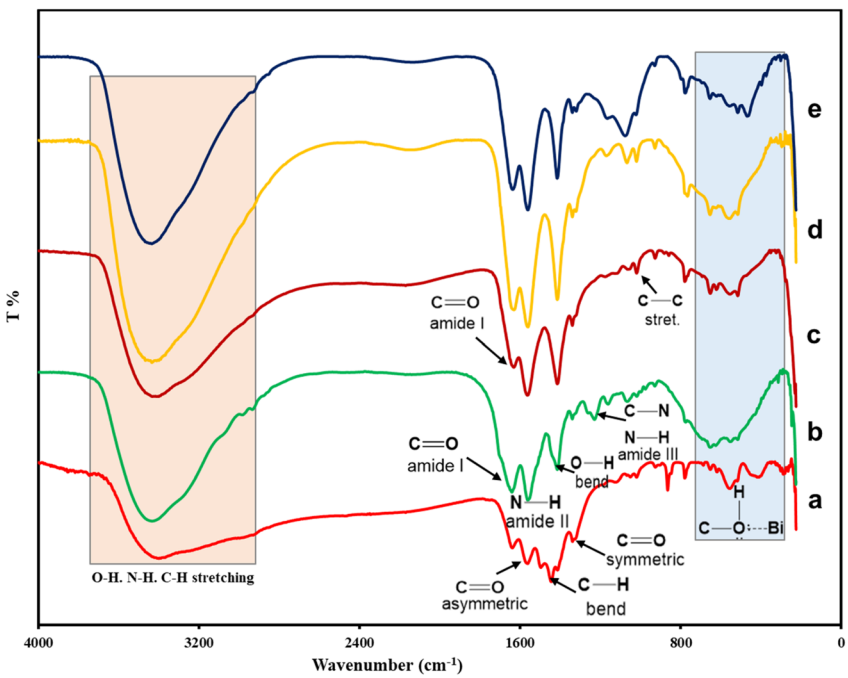

Fig. 3 FTIR spectra of (a) bare Bi and (b) SF and the Bi/SF nanointerfaces with different weight ratios of (c) 6 : 1, (d) 4 : 1, and (e) 2 : 1 of Bi and SF.

binding. For instance, the amide II band at 1510–1560 cm^{-1} corresponds to N–H bending and C–N stretching. The amide III band at 1230–1300 cm^{-1} arises from C–N and C–O stretching coupled with N–H bending. Additional peaks in the 1000–1250 cm^{-1} region are attributed to C–O stretching of phenolic, alcoholic or ether groups of C–O–C linkages. Notably, the intensity of the amide I and II bands increased with higher fibroin content (2 : 1 ratio), confirming stronger protein coating, while in the 6 : 1 ratio spectrum, the relative weakening of these bands suggests thinner fibroin coverage. Residual nitrate signatures (1384 and 824 cm^{-1}) are absent in coated samples, indicating complete reduction of Bi^{3+} ions and stabilization by SF. Collectively, these spectral features demonstrate that SF provides a robust organic shell around Bi, with coating thickness and conformational state modulated by the Bi : SF ratios.

3.3 D_h, surface morphology, and average sizes of Bi/SF

D_h of bare Bi and Bi/SF with different Bi : SF weight ratios (2 : 1, 4 : 1, and 6 : 1) was evaluated using the DLS method, as shown in Fig. S2. The D_h values increased as the amount of Bi in Bi/SF increased. The surface morphology of the bare Bi and Bi/SF nanointerfaces is shown in Fig. 4. The SEM image of bare Bi (Fig. 4a) revealed quasi-spherical particles with pronounced agglomeration and rough surfaces, with an average diameter of 207 nm. In contrast, Bi/SF nanointerfaces (Fig. 4b, prepared at a 2 : 1 Bi : SF ratio) exhibited spherical particles with smoother and more regular surfaces compared to bare Bi, and an average diameter of 88 nm. The improved dispersion and reduced surface roughness demonstrate the stabilizing effect of SF, which provides steric and entropic barriers to aggregation. At a 4 : 1 Bi : SF ratio (Fig. 4c), the particles (97 nm) displayed minimal aggregation with moderate inter-particle separations, reflecting partial stabilization. At a 6 : 1 Bi : SF ratio (Fig. 4d), the particles appeared larger (117 nm), aggregated and occasionally coalesced into domains, indicating insufficient polymer passivation at higher Bi-loadings. These morphological trends highlight the critical role of the SF concentration in controlling nucleation, growth, and stabilization of core Bi. Lower Bi : SF ratios favor discrete, uniformly distributed particles with enhanced catalytic accessibility, while higher ratios yield thicker SF shells that improve colloidal stability but reduce surface accessibility. Biopolymer coatings often reduce aggregation and polydispersity relative to uncoated particles, where SF adsorption provides steric/entropic barriers to coalescence while preserving nanoscale morphology.[21–23]

TEM micrographs (Fig. 5) provide complementary evidence to the SEM observations, confirming the influence of SF concentration on Bi nanoparticle morphology and stabilization.[56] Bare Bi (Fig. 5a) appears as quasi-spherical particles (203 nm) with broad size variation, consistent with the clustering and regular surfaces shown in SEM. At a 2 : 1 Bi : SF ratio (Fig. 5b), the TEM micrograph reveals discrete spherical nanoparticles (89 nm) with larger shells, corroborating the SEM evidence of relatively smoother surfaces and improved dispersion. This morphology reflects effective steric stabilization by SF, which reduces aggregation and enhances catalytic accessibility.[55,56] At a 4 : 1 Bi : SF ratio (Fig. 4c), particles (96 nm) show thinner shells, in agreement with the SEM findings of intermediate stabilization and partial clustering, representing a balance between activity and stability. Fig. 5d highlights (a 6 : 1 Bi : SF ratio) larger particles (116 nm) with irregular shells and occasional coalescence, consistent with SEM evidence of thinnest coatings and aggregation, indicating that higher Bi loading favors colloidal stability and recyclability at the expense of surface accessibility. Therefore, TEM results confirm that SF-concentration leads to tuning particle size, shell thickness, and dispersion stability.

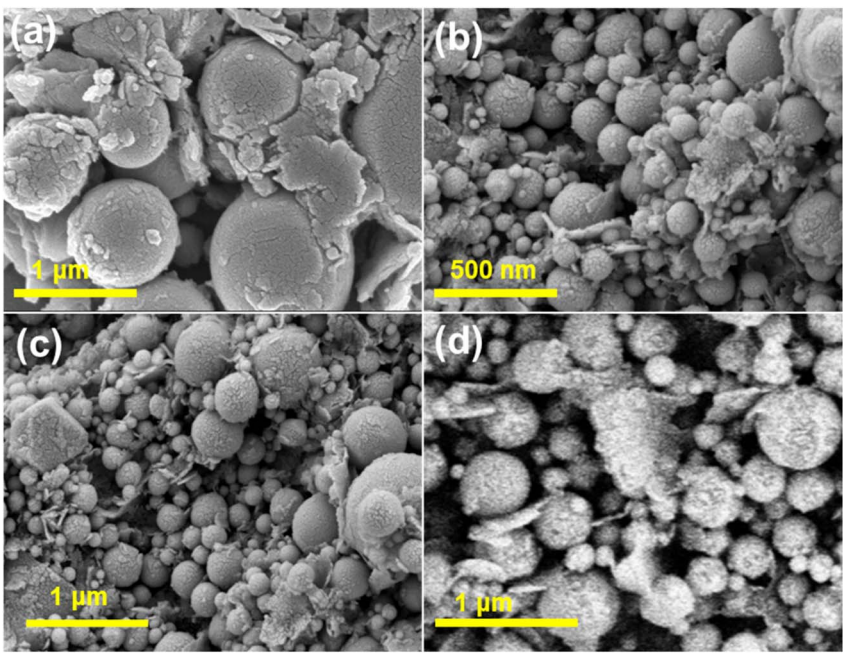

Fig. 4 SEM images of (a) bare Bi and the Bi/SF nanointerfaces with different weight ratios of (b) 2 : 1, (c) 4 : 1, and (d) 6 : 1 of Bi and SF.

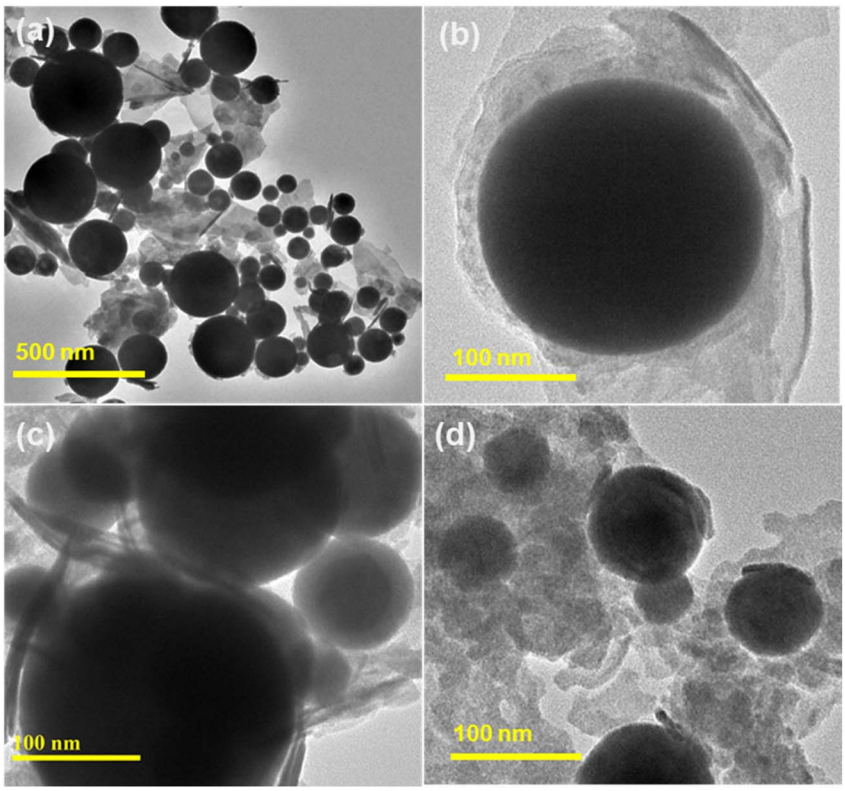

Fig. 5 TEM images of (a) bare Bi and the Bi/SF nanointerfaces with different weight ratios of (b) 2 : 1, (c) 4 : 1, and (d) 6 : 1 of Bi and SF.

3.4 Optical properties, crystal structure and crystallite size

The UV–vis absorption spectra of the synthesized bare Bi and Bi/SF nanointerfaces with different weight ratios of Bi and SF (2 : 1, 4 : 1, and 6 : 1) are shown in Fig. 6a. Bare Bi exhibited an absorption band at 246 nm, which is very similar to reported absorption bands for bismuth particles.[58] However, the bare Bi exhibited the highest intensity due to inter-band transitions of rhombohedral-Bi and strong scattering from larger aggregates. SF-coated Bi displayed progressively attenuated and slightly red-shifted profiles as the organic shell increased (2 : 1 > 4 : 1 > 6 : 1 in

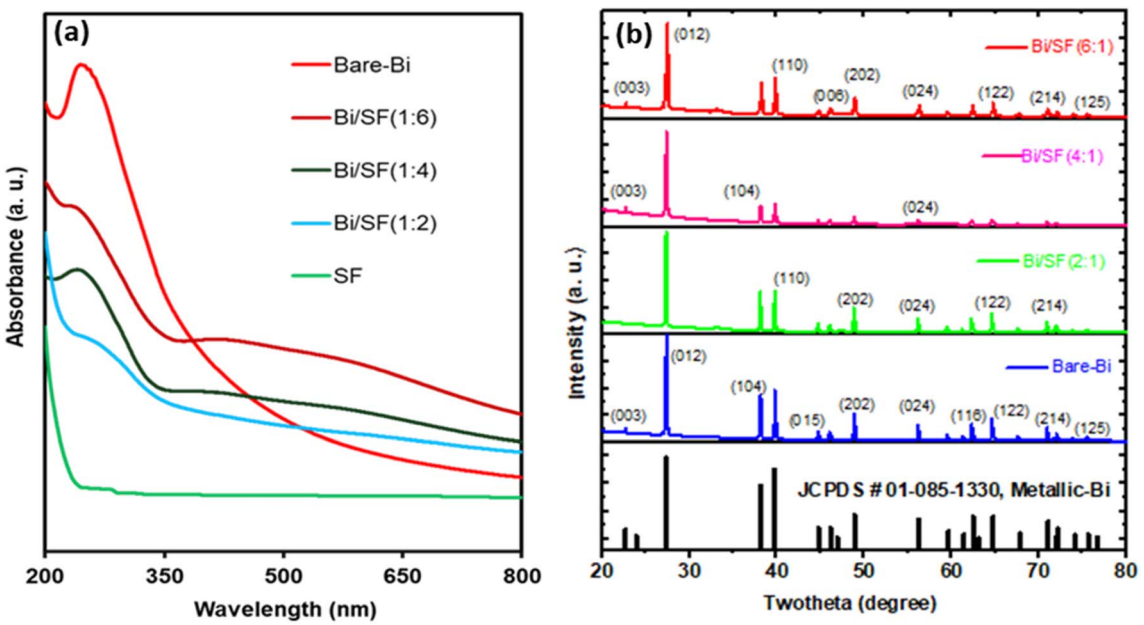

Fig. 6 (a) UV-vis spectra of SF, bare Bi and the different Bi/SF nanointerfaces. (b) PXRD patterns of bare Bi (blue) and the Bi/SF nanointerfaces prepared using 2 : 1 (bright green), 4 : 1 (pink), and 6 : 1 (red) weight ratios of Bi and SF.

intensity), consistent with the dielectric screening and improved dispersion imparted by SF.[56] The pure-SF spectrum is featureless over the measured range, confirming that the observed bands arose from only Bi rather than the proteinaceous SF-matrix.

Fig. 6b shows the standard PXRD patterns of reference Bi (black) and the experimental PXRD patterns of bare Bi (blue) and Bi/SF nanointerfaces with 2 : 1 (light green), 4 : 1 (pink) and 6 : 1 (red) weight ratios of Bi and SF. In the PXRD profile of bare Bi, some characteristic reflections are centered at 22.64°, 27.38°, 38.14°, 39.80°, 44.70°, 46.17°, 48.85°, 56.18°, 62.34°, 64.68°, 67.62°, 70.95°, and 75.46°. These peak positions are assignable to the Bravais lattice planes of (003), (012), (104), (110), (015), (006), (202), (024), (116), (122), (214), and (115), respectively, for the rhombohedral crystal structure of Bi-unit cells. All these signal positions are in good agreement with those of Bi reported in the literature (JCPDS file No. 01-085-1330).[30,54–56] The high intense and sharp diffraction signal at 27.25° is a clear indication of metallic Bi.[30] The diffraction signals of all the Bi/SF nanointerfaces were centered almost identically to those of metallic Bi. No undesirable peaks were observable in the PXRD patterns related to the bismuth oxide phases, indicating that the bare Bi and all Bi/SF interfaces have identical crystal structures and are fully composed of metallic Bi atoms. The core Bi in Bi/SF interfaces has an A7 structure in the hexagonal setting. The space group was R-3m (No. 166), which contributed to the formation of a hexagonal prismatic unit cell. The unit cell parameters were found to be $a = b = 4.53962$ Å, $c = 11.78000$ Å with $\alpha = \beta = 90°$, and $\gamma = 120°$. The Bravais lattice is rhombohedral (R) expressed in hexagonal axes, yielding a threefold rotation axis along c and forming layered stacking along the c-direction. No deterioration occurred in the rhombohedral structure of core Bi during treatment with different ratios of Bi and SF for functionalization and stabilization. The Debye–Scherer formula (eqn (4)) was used to calculate the average crystallite size of bare Bi and core–shell Bi/SF nanointerfaces.

$$D = k \times \lambda/\beta \cos(\theta), \quad (4)$$

where D is the average crystallite size; k is the shape factor, whose value is 0.9; the wavelength of the X-ray radiation is λ; the Scherrer constant is 0.15406; θ is the Bragg's diffraction angle; and β is the full width at half maximum (FWHM) of the respective peak in the PXRD pattern. The average crystallite sizes of bare Bi and the Bi/SF nanointerfaces with weight ratios of 2 : 1, 4 : 1, and 6 : 1 were calculated to be 208 nm, 89 nm, 95 nm, and 115 nm, respectively. The average particle sizes of the bare Bi and Bi/SF (2 : 1, 4 : 1, and 6 : 1) nanointerfaces measured by DLS (Fig. S2) were quite higher, as they were measured in an aqueous dispersion state. This enhancement of these hydrodynamic sizes is due to the hydrophilic SF-coating and develops hydration layer boundaries on the surface of the Bi-cores. SEM and TEM analyses were performed in the dry state of the samples, and the results are consistent with the crystallite sizes obtained from the PXRD analysis.

3.5 Crystallinity and phase of core Bi

High resolution transmission electron microscopy (HRTEM) micrographs provide direct evidence for the crystalline nature

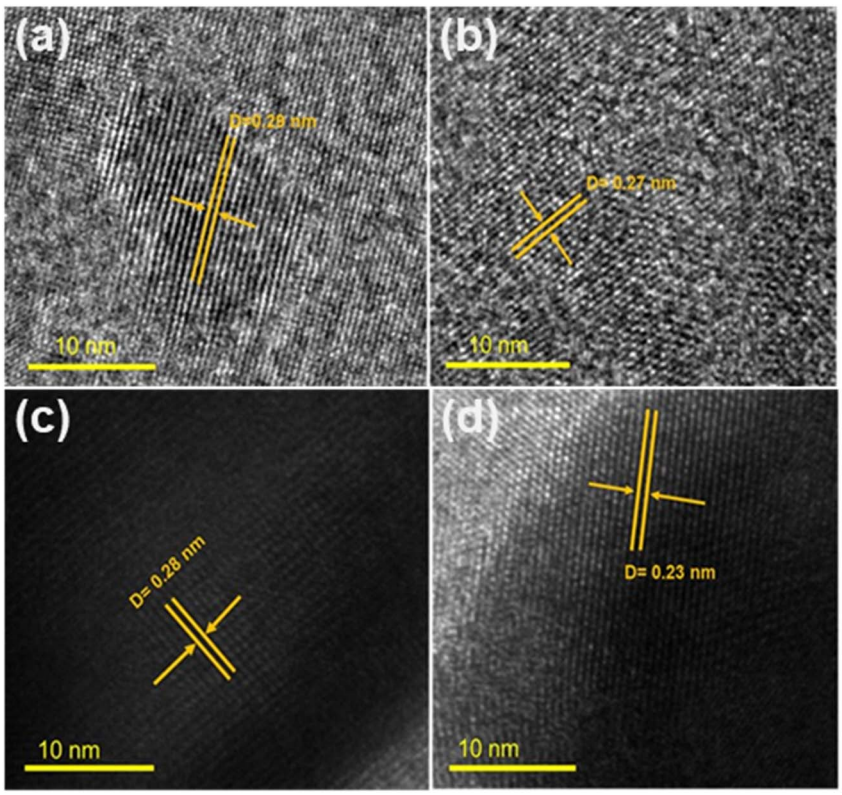

Fig. 7 HRTEM micrographs of (a) bare Bi and the Bi/SF nanointerfaces having (b) 2 : 1, (c) 4 : 1, and (d) 6 : 1 Bi to SF weight ratios.

and structural modulation of core Bi upon SF-coating at varying Bi : SF ratios. Fig. 7a depicts well-defined lattice fringes for bare Bi, with an interplanar spacing of 0.28 nm, corresponding to the (012) plane of rhombohedral Bi (space group $R\bar{3}m$), consistent with standard crystallographic data and recent reports on uncoated-Bi.[30,55,56] Fig. 7b, representing the 2 : 1 Bi : SF ratio, shows slightly reduced spacing at 0.27 nm, suggesting subtle lattice compression likely due to surface interaction with SF's polar groups. Fig. 7c shows that the interplanar spacing (0.28 nm) is retained for a 4 : 1 ratio, indicating stable crystalline domains with moderate organic SF-coverage. In contrast, Fig. 7d, corresponding to the 6 : 1 ratio, demonstrates a reduced interplanar spacing of 0.23 nm. This reflects increased surface strain or partial lattice distortion due to the least amount of SF, which is insufficient passivation and stronger interparticle interactions. These variations in *d*-spacing indicate surface-induced lattice perturbations and are consistent with recent studies, showing that protein or polymer coatings can modulate the surface energy and crystallographic parameters of core Bi.[24] The preservation of lattice fringes across all samples confirms the retention of the metallic core Bi, while the observed shifts in interplanar spacing highlight the influence of SF-concentration on nanoparticle surface structure and crystallinity.

Crystalline phase purity was further analyzed using a selected area electron diffraction (SAED) pattern. Fig. 8 shows the SAED patterns of bare Bi (a) and Bi/SF nanointerfaces with Bi to SF weight ratios of (b) 2 : 1, (c) 4 : 1, and (d) 6 : 1. The fine Debby-Scherrer ring structure confirmed the polycrystalline nature of bare Bi and all the Bi/SF nanointerfaces.[55,59] The calculated diffraction rings are assignable to the Bravais lattice planes and *d*-spacing values from the SAED pattern resembling the various planes of the bare Bi and Bi/SF interfaces. The SAED patterns confirmed polycrystalline rhombohedral-Bi having a space group R-3m across bare Bi and Bi/SF nanointerfaces, with concentric Debye–Scherrer rings indexed to Bi-lattice planes and modest variations in ring sharpness that reflect SF-modulated crystallite coherence. For bare Bi (Fig. 8a), rings assigned to (119), (202), and (104) indicate well-developed crystalline domains consistent with metallic Bi.[30] The relative intensity and continuity of these rings suggest broad yet coherent grain distributions typical of bare Bi. In 2 : 1, Bi : SF nanointerfaces (Fig. 8b), rings indexed to (306), (113), and (104) remain crisp, evidencing preserved Bi-crystallinity under a uniform SF-shell. The presence of higher-index planes like (306) indicates diversifying domains, in line with restrained aggregation and enhanced dispersion. The 4 : 1 sample (Fig. 8c) displays rings corresponding to (202) and (012), maintaining the rhombohedral signature while showing slightly increased ring breadth. This indicates a reduced coherent domain size under intermediate SF-coverage. The 6 : 1 sample (Fig. 8d) exhibits rings for (214), (113), and (104), with comparatively sharper features that are consistent with larger crystallites and more pronounced interparticle coupling due to thinner SF-passivation. The plane assignments align with standard-Bi powder diffraction data and corroborate PXRD indexing and HRTEM lattice fringes ($d = 0.28$ nm for (012)/(104)).[30,56,59] These results collectively confirm that SF-coatings preserve the metallic Bi phase while modulating nanocrystal size and orientation distributions.

3.6 Surface porosity of Bi/SF

The nitrogen adsorption–desorption isotherm of typical Bi/SF nanointerfaces was measured at 77 K, as shown in Fig. 9. These isotherms exhibit characteristic Type-IV profiling (Fig. 9a). According to the IUPAC classification, this is indicative of the mesoporous behavior of the Bi/SF nanointerfaces. A distinct hysteresis loop is observed between the adsorption and

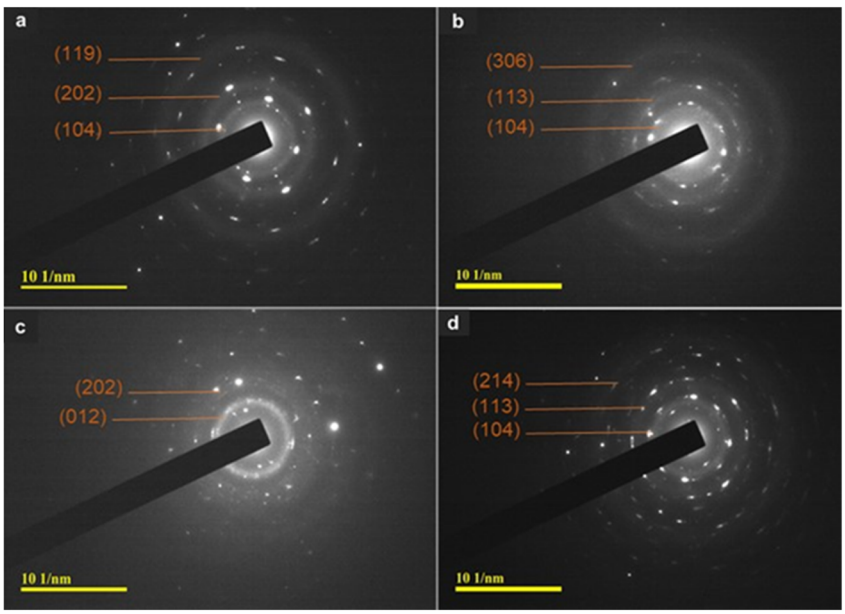

Fig. 8 SAED patterns of the synthesized (a) bare Bi and Bi/SF nanointerfaces having (b) 2 : 1, (c) 4 : 1, and (d) 6 : 1 Bi to SF weight ratios.

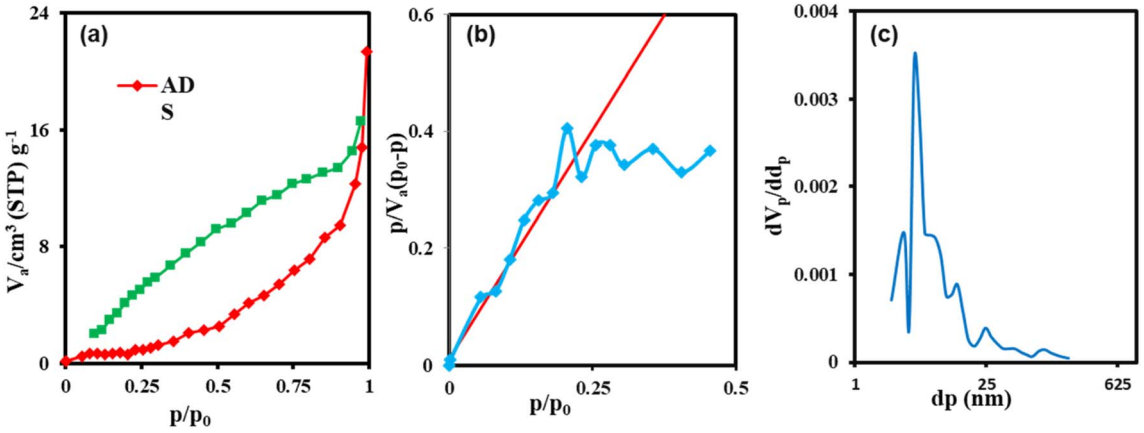

Fig. 9 (a) Typical N_2 adsorption–desorption isotherms measured at 77 K, (b) BET surface area analysis, and (c) BJH pore size distribution of the Bi/SF (2 : 1) nanointerfaces.

desorption branches, confirming the presence of capillary condensation within mesopores. The hysteresis loop corresponds to the H2-type, which is typically associated with ink-bottle-shaped pores. The pore networks exhibit pore blocking and percolation effects.[54,56,59] The adsorption branch shows a gradual uptake at lower relative pressures ($P/P_0 < 0.1$), suggesting limited microporosity. A steep increase in adsorbed volume is observed in the intermediate region (P/P_0, 0.4–0.8), followed by saturation at $P/P_0 \approx 1$. The desorption branch displays a delayed release of nitrogen, consistent with constricted pore necks and complex pore connectivity. The specific surface area was calculated using the Brunauer–Emmett–Teller (BET) method within the relative pressure range of 0.05–0.30. The BET plot (Fig. 9b) exhibited excellent linearity with a correlation coefficient ($R^2 > 0.99$), confirming the applicability of the BET model. From the slope and intercept of the BET plot, the monolayer capacity (V_m) and BET constant (C) were calculated as 0.6332 cm^3 (STP) g^{-1} and 130.7, respectively. BET analysis revealed a specific surface area of 52.4 m^2 g^{-1}, markedly higher than that of bare Bi (12.7 m^2 g^{-1}) and metallic Bi-based materials, confirming the role of SF in preventing aggregation and exposing additional active sites.[54–56] The total pore volume was estimated from the amount of nitrogen adsorbed at $P/P_0 \approx 0.99$. The pore size distribution was evaluated using the Barrett–Joyner–Halenda (BJH) method applied to the desorption branch of the isotherm. The BJH curve (Fig. 9c) exhibits a pronounced peak centered at 4 nm, confirming the mesoporous nature of the nanointerfaces. The distribution is unimodal and relatively narrow, suggesting a uniform pore architecture.[54,59] The gradual decline in pore volume beyond 4 nm indicates the presence of a minor fraction of larger mesopores or interparticle voids. These mesopores are ideally suited for substrate preconcentration and rapid diffusion, thereby facilitating hydride transfer during catalytic reduction. The structural features observed here are consistent with the SEM and TEM data, which showed quite rougher surfaces and improved dispersity. Together, these results demonstrate that the conformal SF-shell stabilizes core Bi and introduces accessible mesoporosity, enabling reproducible catalytic activity and recyclability. The synergy between surface area enhancement, mesopore uniformity, and colloidal stability explains the superior performance of Bi/SF nanointerfaces with a ratio of 2 : 1 compared to oxide-based or carbon-based supported catalysts.[39,45,51,52] Therefore, we selected Bi/SF (2 : 1) nanointerfaces to evaluate catalytic performances in reducing azo and nitro groups containing organic pollutants, as systematically outlined in the next section.

3.7 Catalytic potentials of Bi/SF nanointerfaces

The catalytic performance of Bi/SF nanointerfaces for CR, MO, EBT and *p*-NA reductions was evaluated under ambient conditions using both visual and spectroscopic methods, and the results are shown in Fig. 10. When only $NaBH_4$ was added to the CR solution, about <1% catalytic reduction occurred even after 40 min. However, in the presence of Bi/SF catalytic nanointerfaces, CR was reduced *via* decolorization and reached 100% within 3 min (Fig. 10a). The aqueous solution of CR showed two strong absorption bands for $\pi \rightarrow \pi^*$ at 500 nm and for $n \rightarrow \pi^*$ transition at 350 nm, which are related to the two –N=N– groups, as shown in Fig. 10b.[60] The intensity of these two peaks decreased gradually due to the reduction of CR concentration and generated a new peak at 282 nm. Initially, $NaBH_4$ reduced the –N=N– groups of CR and produced hydrazine derivatives in the presence of Bi/SF.[19,44] The intensity of this peak increased and moved to 255 over time.

Optical images reveal that MO alone and MO + $NaBH_4$ remain intensely colored even after 45 min, confirming the inability of $NaBH_4$ to reduce MO without a catalyst (Fig. 10c and d).[41–43] In contrast, the addition of Bi/SF leads to complete decolorization, indicating rapid and efficient catalytic reduction. MO follows a similar trend, with complete reduction achieved in 4 min, and *p*-NA reduction proceeds slightly slower and is completed in 5 min (Fig. 10e and f). The fastest reduction was observed for EBT, as shown in Fig. S3. In all cases, UV-vis spectra show a monotonic decrease in absorbance without the emergence of intermediate peaks, suggesting a clean reduction pathway. Mechanistically, Bi/SF operated *via* a synergistic dual-function model; the core Bi facilitated electron transfer from

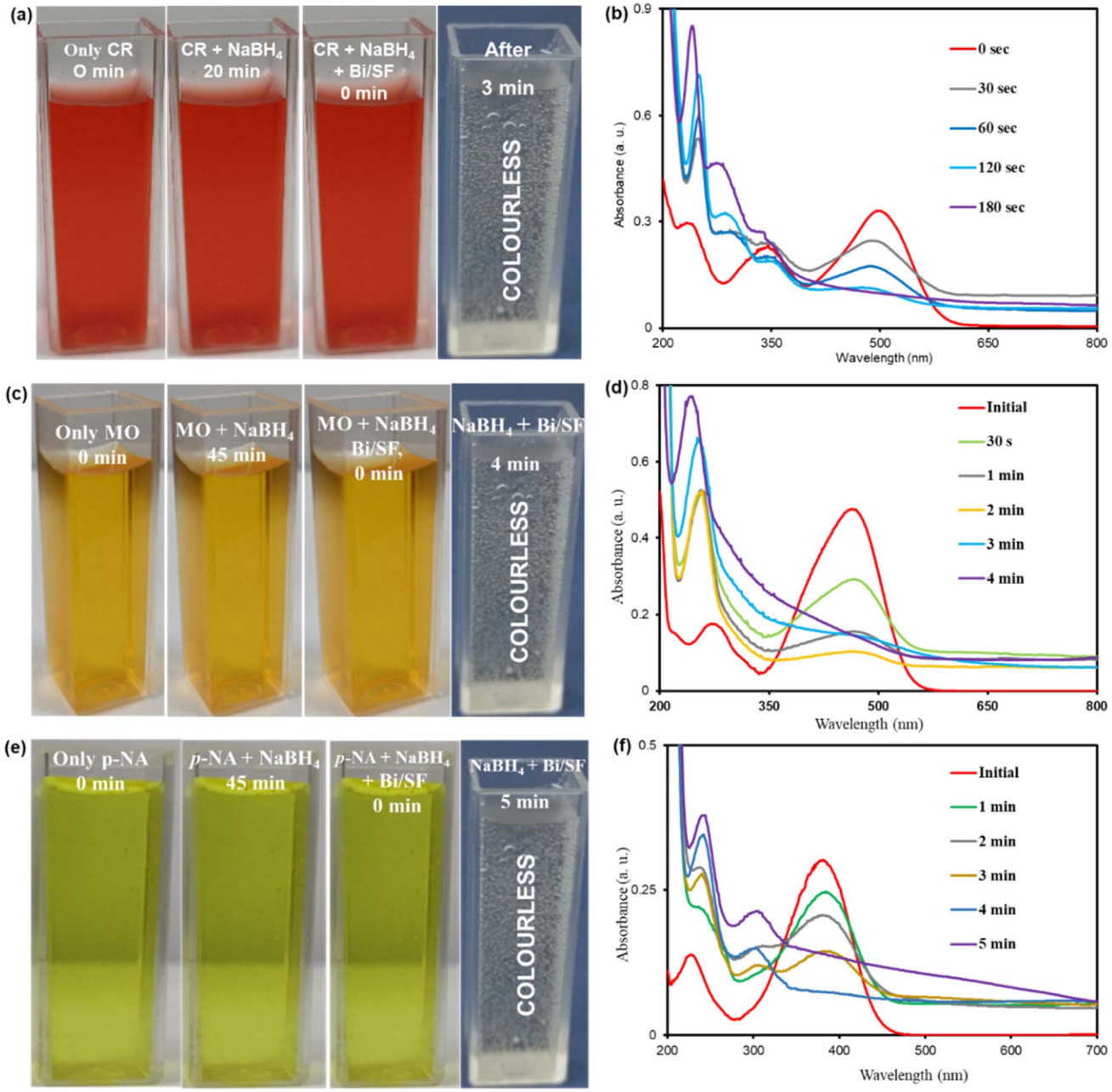

Fig. 10 Optical images for the visualization of the color changes (a), (c), and (e) and the time-dependent UV-vis spectra for the catalytic reduction (b), (d), and (f) of CR, MO and *p*-NA, respectively. Conditions: 25 °C, CR: 30 mg L^{-1}, MO: 7 mg L^{-1}, *p*-NA: 0.06 mM, $NaBH_4$: 0.5 mg, catalyst: 0.2 mg, and volume: 50 mL.

BH_4^- to the dye molecule, while the SF-shell enhanced colloidal stability and provided peptide-based adsorption sites that pre-concentrate the substrate near the catalytically active domains. The SF-matrix also prevents nanoparticle aggregation, maintaining a high clean surface area and accessibility. The reduction of azo dyes (CR, MO and EBT) involves the hydrogenation of the –N=N– bond. However, *p*-NA reduction targets the $-NO_2$ group; both groups proceeded *via* surface-mediated electron relay and protonation steps.[52,53] The observed substrate-dependent kinetics and clean spectral transitions are consistent with recent reports.[43–54]

3.8 Optimization of reduction parameters and catalytic efficiency

The catalytic reduction parameters were systematically optimized by varying the reduction time, pH of the reaction medium, and substrate concentration. The goal was to identify the most efficient conditions for complete reduction with the minimal reagents used and to reach rapid kinetics. Across all systems, $NaBH_4$ alone showed negligible activity, while the introduction of Bi/SF catalytic nanointerfaces led to rapid and complete decolorization. Substrate concentration also played

a critical role. Moderate loads of substrates (25–35 mg L^{-1}) ensured rapid kinetics, while higher concentrations slowed reduction due to limited surface accessibility and electron flux. The Bi/SF interfaces exhibited the fastest kinetics for CR, with complete reduction within 4 min at 20 mg L^{-1}, as shown in Fig. 11a. With increasing CR concentration, the reaction time increased. This reduction reflects the high susceptibility of the diazo chromophore to electron relays at the Bi/SF nanointerfaces. The MO reduction followed the CR reduction closely, achieving a full reduction (4 min) under identical conditions (Fig. 11b). However, its azo structure required slightly longer times than CR. In contrast, *p*-NA reduction was slower, reaching completion in 6 min at 25–30 mg L^{-1} and pH 9, consistent with the higher electron demand of nitro group conversion to amines (Fig. 11c). Optimal performance was consistently observed under mildly basic conditions (Fig. 11d–f), which stabilized BH_4^- and enhanced substrate adsorption. Acidic conditions consumed BH_4^- prematurely, while strongly basic media reduced dye-SF interactions. Substrate concentration also played a critical role: moderate loads (25–35 mg L^{-1}) ensured rapid kinetics, while higher concentrations slowed reduction due to limited surface accessibility and electron flux.[54,56] Optimal performance was consistently observed under mildly acidic conditions (pH 6), which relatively stabilized BH_4^- and enhanced substrate adsorption. However, strong acidic conditions consumed BH_4^- prematurely, while strongly basic media reduced dye-SF interactions. CR reduction was most efficient, followed by MO and *p*-NA, reflecting structural differences in azo *versus* nitro functionalities.

Under optimized conditions (25 °C, 0.2 mg Bi/SF, 0.50 mg $NaBH_4$, and pH 9.0), the catalytic reduction of CR, MO, and p-NA revealed distinct substrate-dependent behaviors in terms of efficacy, as shown in Fig. 11g–i. In the reduction of CR, Bi/SF interfaces showed the fastest and highest reduction efficiency (99%) in just 3 min at 30 mg L^{-1}, and this performance remained almost consistent up to 90 mg L^{-1} (Fig. 11g).[48–52] This high efficiency is due to the presence of high conjugated dual azo moieties and strong adsorption affinity to the SF-shell, which was activated by facilitating rapid electron transfer to the chromophore, –N=N– and cleavage of CR. MO has an azo linkage and sulfonate groups, which were reduced to 97% at 35 mg L^{-1}, as shown in Fig. 11h. MO reduction efficiency decreased with increasing concentration.[42,43] At 210 mg mL^{-1}, the reduction efficiency reached up to 62% and exhibited relatively slower efficiency due to the reduced adsorption and lesser electron demand in the MO structure. In contrast, EBT bearing sulphonic acid and O–H groups exhibited 73% reduction at 40 mg L^{-1} (Fig. 11i). The reduction efficiency reached a maximum (83%) at 80 mg mL^{-1}, and a slight decline was observed at the highest concentration because of azo-to-amine conversion, leading to weaker initial adsorption to Bi/SF nanointerfaces.[39,40] Overall, in all tested concentrations, CR showed consistent viability, MO displayed a dose-dependent decline, and EBT peaked at intermediate concentrations, suggesting that all reductions were efficient. These results collectively validate Bi/SF nanointerfaces as a versatile and selective catalyst system with CR > MO > EBT in reduction efficiency and tunable performance based on substrate structure and reaction conditions. The reduction kinetics for CR, MO, *p*-NA and EBT were quantitatively analyzed through linear regression, $\ln(A/A_0)$ *versus* time, as shown in Fig. S4.

3.9 Plausible reduction mechanism

Bi/SF nanointerfaces catalyze azo and nitro group reductions by coupling interfacial substrate preconcentration with metal-surface hydride chemistry.[55–59] The active functionalities like –NH, $–NH_2$, $–CO_2^-$, –SH, –OH, and aromatic residues present in peptide domains of SF adsorbed and oriented the azo moieties and nitroaromatics *via* hydrogen bonding, electrostatic attractions, and π–π stacking contacts. These interactions mainly facilitate the positioning of the electrophilic bonds adjacent to the core Bi. $NaBH_4$ delivered hydride equivalents that formed transient surface species, $Bi–H_{ads}$, while the Bi^0 lattice acted as an electron reservoir that injected preferential charge into the substrate antibonding orbitals to weaken the –N=N– and $–NO_2$ moieties.[56] The successive electron/hydride transfers yield hydrazo (–HN–NH–) intermediates and ultimately convert into anilines for azo groups. The nitro groups pass through nitroso and hydroxylamine intermediates en route to the amines for nitroaromatics. The products were less strongly bound to the interfacial SF-shell, desorbed into the solution, and the clean Bi^0 surface was regenerated by continued hydride supply.[56] The SF-shell prevents oxidation/agglomeration and maintains high turnover and pseudo-first-order kinetics under excess $NaBH_4$.[61] The detailed reactions involved in the catalytic reduction of azo and nitro moieties are mentioned below:

Hydride activation and surface hydride formation:

$$NaBH_4 + 2H_2O \rightarrow NaBO_2 + 4H_2\uparrow$$

$$SF/Bi_{(surf)}{}^0 + H^- \rightleftharpoons SF/Bi–H_{(ads)}$$

SF-mediated adsorption (preconcentration at the shell):

$$Substrate_{(aq)} \rightleftharpoons Substrate_{(SF\text{-}shell)}\ [\textit{via}\ \text{H-bonding, electrostatics, and } \pi–\pi \text{ stacking}]$$

Azo group reduction:

$$R–N{=}N–R' + 2\ SF/Bi–H_{(ads)} \rightarrow R–NH–NH–R'$$

$$R–NH–NH–R' + 2\ SF/Bi–H_{(ads)} \rightarrow R–NH_2 + R'\text{-}NH_2$$

Nitro-group reduction:

$$Ar'–NO_2 + 2SF/Bi–H_{(ads)} \rightarrow Ar'–NO + H_2O$$

$$Ar–NO + 2SF/Bi–H_{(ads)} \rightarrow Ar'–NHOH$$

$$Ar'–NHOH + 2SF/Bi–H_{(ads)} \rightarrow Ar'–NH_2 + H_2O$$

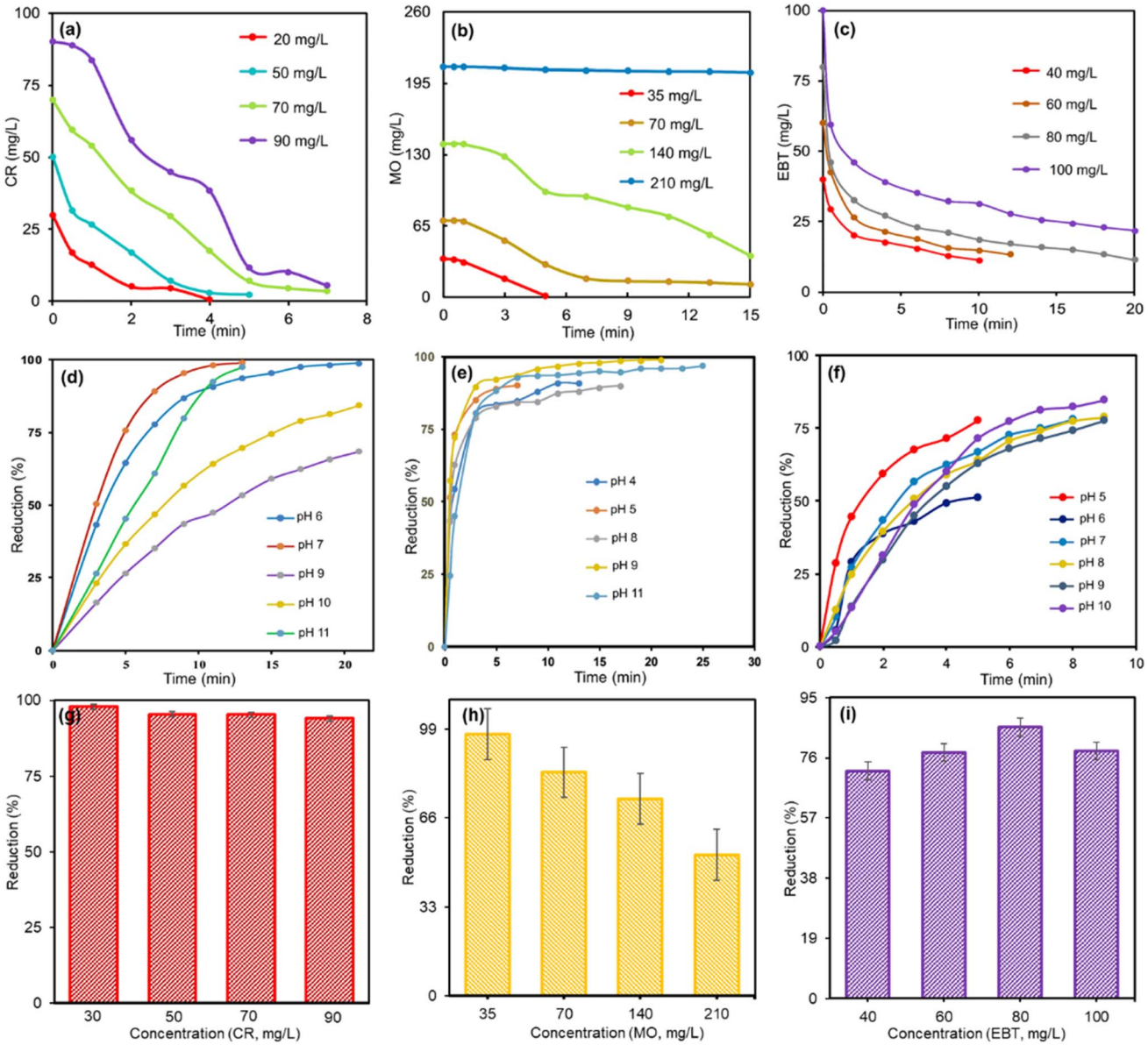

Fig. 11 Optimization of the CR, MO and EBT reduction parameters: (a–c) catalyst contact time, (d–f) pH variation, and (g–i) substrate concentration. Conditions: 25 °C, catalyst: 0.2 mg, $NaBH_4$: 0.5 mg, and volume: 50 mL. The mean values from the triplicate measurements are shown in the data, with corresponding error bars indicating standard deviations (±5%).

Product desorption and catalyst regeneration:

$$\text{Products}_{(\text{SF-shell})} \rightarrow \text{Products}_{(\text{aq})}$$

$$\text{SF/Bi–H}_{(\text{ads})} + \text{H}_2\text{O/Substrate} \rightarrow \text{SF/Bi(surf)}^0 \text{ (ready for next cycle).}$$

3.10 Reusability and post catalytic stability of Bi/SF nanointerfaces

For sustainability and environmental and circular economic perspectives, the recycling and reusability of any catalysts are highly desirable.[56,61] Herein, recycling experiments were conducted using a simple low-speed centrifugal washing process to verify and monitor sustainability. The long-term reusability for the catalytic reduction efficiencies of Bi/SF nanointerfaces is shown in Fig. 12 and in S5. The obtained results indicate that the catalytic reduction efficacy for both the azo and nitro groups is very high. The reduction efficiencies of Bi/SF for the azo group in CR remained about 94% to 92% after five repetitive cycles. For the azo groups in MO, the reduction potential was also rendered within 90% under all repetitive cycles. The reduction ranged from 83% to 72% in the successive five-step process for the azo groups in the EBT. On the contrary, the catalytic efficiencies of Bi/SF nanointerfaces for *p*-NA oscillated from 91% to 80%. A negligible efficiency loss in reducing the azo groups was observed, while about 10% efficiency decreased for *p*-NA. The decrease in reduction efficiencies is due to the plausible minor

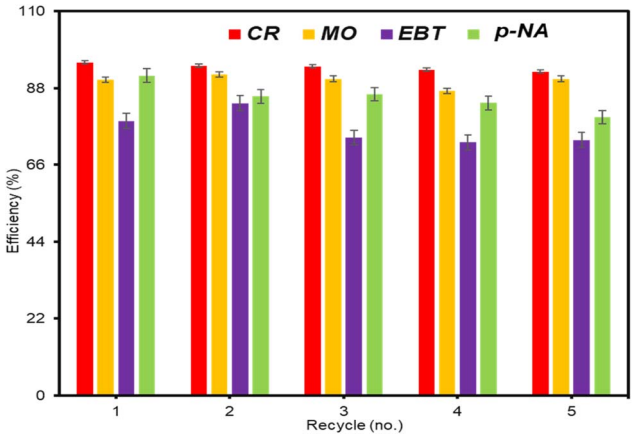

Fig. 12 Recyclability of the catalytic Bi/SF (2 : 1) nanointerfaces in reducing (a) CR, (b) MO. (c) EBT, and (d) *p*-NA in the presence of $NaBH_4$. Conditions: 25 °C, catalyst: 0.2 mg, $NaBH_4$: 0.5 mg, and volume: 50 mL. Each measurement is performed in triplicate and the mean values are shown with error bars having standard deviations (±5%).

changes in active sites in the Bi/SF catalyst nanointerface as well as multiple usage in successive catalytic reactions.[56,61] FTIR and PXRD analyses confirmed post catalytic stability of the recycled nanointerfaces with negligible structural change (Fig. S5).

4. Conclusions

This study successfully develops a new catalytic nanointerface production method using Bi^{3+} ions and dissolved-SF with enhanced dispersity, crystallinity, and environmental friendliness over traditional catalysts. This synthesis protocol is superior because it does not involve poisonous reagents like highly concentrated $LiBi \cdot 2H_2O$ (9.3 M) for SF dissolution. Therefore, this protocol does not require tedious membrane purification of the dissolved-SF nor the use of any toxic surfactants and solvents, and enables easy transformation of SF dispersity. The synthesis and functionality of Bi/SF nanointerfaces were confirmed spectroscopically. Rhombohedral geometry, responsive-morphology and surface, enhanced dispersity and core–shell nanointerfaces established dominant interfacial activity. The Type-IV isotherm with an H2 hysteresis loop indicates ink-bottle-shaped mesopores, while the BET and BJH results provide quantitative evidence of significant surface area and pore volume. The catalysis study revealed that Bi/SF nanointerfaces functioned as effective and recyclable nanocatalysts for the reduction of structurally diverse organic azo and nitro-pollutants. The SF-shell plays a critical role in stabilization, substrate adsorption, anti-fouling behavior, and product diffusion, while core Bi ensures rapid electron relay from $NaBH_4$ to the targeted functional groups. This system consistently delivers faster, cleaner reductions and maintains high activity across multiple cycles without a significant loss of performance. Parameter optimization studies demonstrated that reduction was strongly influenced by pH, contact time, and initial substrate concentration, with maximum reduction achieved under mildly acidic conditions. The substrate-dependent kinetics (CR > MO > p-NA) reflect the interplay between molecular structure, adsorption affinity, and electron demand, while recyclability data confirm the robustness of the Bi/SF nanointerfaces. Beyond dye and nitroaromatic reduction, the design principles demonstrated herein are biopolymer stabilization, electron relay, and adsorption-driven selectivity, which offer a blueprint for nanocatalysts in environmental and industrial chemistry. Bi/SF nanointerfaces stand as a benchmark for next-generation biopolymer-metal nanohybrids in sustainable remediation, with broad implications for wastewater treatment, detoxification of industrial effluents, and site-specific catalytic systems.

Conflicts of interest

The authors have no competing financial interests to declare.

Data availability

The data collected from this study were mostly added to the main manuscript and supplementary information (SI). The necessary data are available from the corresponding author upon proper request.

Supplementary information: Table S1 and Fig. S1 to S6, the element%, DLS profiles, EBT reduction and reduction kinetics. See DOI: https://doi.org/10.1039/d6ra02184k.

Acknowledgements

This work was financially supported by the University Grants Commission, Dhaka, Bangladesh (Grant no. 2020-6701731276). The authors acknowledge the FTIR and UV-vis measurement support from the Central Science Laboratory, the University of Rajshahi. The authors also gratefully acknowledge the others support provided by the Faculty of Science, the University of Rajshahi.

References

1 Y. Yuan, Z. Yang, W. Lai, J. Zhang, X. Chen and H. Huang, *Energy Lab.*, 2023, **1**, 220021.
2 N. Suganuma, I. T. Ghampson, H. Miura, J. Murakami, K. K. Bando, T. Kodaira, T. Yamasaki, A. Takagaki, T. Ishihara and T. Shishido, *Catal. Sci. Technol.*, 2023, **13**, 3927–3939.
3 V. Pasindu, P. Yapa, S. Dabare and I. Munaweera, *RSC Adv.*, 2025, **15**, 33162–33186.
4 S. K. Srivastav and N. S. Gajbhiye, *J. Am. Ceram. Soc.*, 2012, **95**, 3678–3682.
5 W. Li, *Mater. Chem. Phys.*, 2006, **99**, 174–180.
6 P. C. Naha, A. A. Zaki, E. Hecht, M. Chorny, P. Chhour, E. Blankemeyer, D. M. Yates, W. R. T. Witschey, H. I. Litt and A. Tsourkas, *J. Mater. Chem. B*, 2014, **2**, 8239–8248.
7 B. S. Rathi, L. S. Ewe, S. Sanjay, S. Sujatha, W. K. Yew, B. R. Baskaran and S. K. Tiong, *Nanotoxicology*, 2024, **18**, 272–298.

8 W. Wazir, Z. Ahmad, S. Zulfiqar, E. W. Cochran, S. Mubarik, T. Kousar, H. Somaily, J. Shim, H. A. Alsalma and M. Aadil, *Ceram. Int.*, 2023, **49**, 262195090.
9 F. Herold, M. J. A. Goemans, P. Cautaerts, B. J. M. Etzold and M. Rønning, *ACS Catal.*, 2026, **16**, 446–463.
10 M. Sia, F. Lin, H. Ni, S. Wang, Y. Lua and X. Meng, *RSC Adv.*, 2023, **13**, 2140–2154.
11 E. R. Swy, A. S. Schwartz-Duval, D. D. Shuboni, M. T. Latourette, C. L. Mallet, M. Parys, D. P. Cormode and E. M. Shapiro, *Nanoscale*, 2014, **6**, 13104–13112.
12 S. Mahmud, M. Z. Sultana, M. N. Pervez, M. A. Habib and H.-H. Liu, *Fibers*, 2017, **5**, 35.
13 A. K. Ilunga, B. B. Mamba and T. T. I. Nkambule, *Appl. Organomet. Chem.*, 2021, **35**, e6050.
14 S. El Hankari, M. Bousmina and A. El Kadib, *Prog. Mater. Sci.*, 2019, **106**, 100579.
15 R. Irmawati, M. N. Noorfarizan Nasriah, Y. H. Taufiq-Yap and S. B. Abdul Hamid, *Catal. Today*, 2004, **95**, 701–709.
16 I. Meydan, A. Aygun, R. N. E. Tiri, T. Gur, Y. Kocak, H. Seckin and F. Sen, *Environ. Sci.: Adv.*, 2024, **3**, 28–35.
17 Q. Cui, A. Yashchenok, L. Zhang, L. Li, A. Masic, G. Wienskol, H. Möhwald and M. Bargheer, *ACS Appl. Mater. Interfaces*, 2014, **6**, 1999–2002.
18 Y. Sha, I. Mathew, Q. Cui, M. Clay, F. Gao, X. J. Zhang and Z. Gu, *Chemosphere*, 2016, **144**, 1530–1535.
19 M. Ismail, M. I. Khan, S. B. Khan, K. Akhtar, M. A. Khan and A. M. Asiri, *J. Mol. Liq.*, 2018, **249**, 153–160.
20 Z. B. Shifrina, V. G. Matveeva and L. M. Bronstein, *Chem. Rev.*, 2019, **120**, 1350–1396.
21 J. M. Palomo, *Chem. Commun.*, 2019, **55**, 9583–9589.
22 Y. Musa and I. B. Bwatanglang, *Sustainable Nanocellulose and Nanohydrogels from Natural Sources*, Elsevier, 2020, pp. 131–154.
23 S. Velpula, S. R. Beedu and K. Rupula, *J. Mater. Sci.: Mater. Electron.*, 2022, **33**, 2677–2698.
24 M. Mato and J. Cornella, *Angew. Chem., Int. Ed.*, 2024, **63**, e202315046.
25 Z. Li, Y. Hu, Z. Miao, H. Xu, C. Li, Y. Zhao, Z. Li, M. Chang, Z. Ma and Y. Sun, *Nano Lett.*, 2018, **18**, 6778–6788.
26 K. Pothula, L. Tang, Z. Zha and Z. Wang, *RSC Adv.*, 2015, **5**, 83144–83148.
27 M. Yarema, M. V. Kovalenko, G. Hesser, D. V. Talapin and W. Heiss, *J. Am. Chem. Soc.*, 2010, **132**, 15158–15159.
28 C. Li, L. Sun, J. Niu, A. A. Reka, P. Feng and H. Garcia, *Catal. Commun.*, 2023, **175**, 106609.
29 A. Riaz, M. Saeed, M. Munir, A. Intisar, S. Haider, S. Tariq and M. Bilal, *Environ. Res.*, 2022, **212**, 113160.
30 X. Luan, J. Jiang, Q. Yang, M. Chen, M. Zhang and L. Li, *Environ. Eng. Manag. J.*, 2015, **14**, 703–707.
31 Y. Wang, J. Guo, L. Zhou, C. Ye, F. G. Omenetto, D. L. Kaplan and S. Ling, *Adv. Funct. Mater.*, 2018, **28**, 1805305.
32 K. Ma, Z.-F. Wu, K.-Z. Chen and S.-L. Qiao, *J. Mater. Chem. B*, 2025, **13**, 2616–2628.
33 G. Guzmán Carissimi, M. G. Montalbán, M. G. Fuster and G. Víllora, in *21st Century Nanostructured Materials*, ed. P. V. Pham, IntechOpen, London, 2021.
34 Z. Li, K. Li, S. Wang and Q. Zhou, *ACS Sustainable Chem. Eng.*, 2025, **13**, 11348–11361.
35 T. P. Nguyen, Q. V. Nguyen, V.-H. Nguyen, T.-H. Le, V. Q. N. Huynh, D.-V. N. Vo, Q. T. Trinh, S. Y. Kim and Q. V. Le, *Polymers*, 2019, **11**, 1933.
36 X. Fei, M. Jia, X. Du, Y. Yang, R. Zhang, Z. Shao, X. Zhao and X. Chen, *Biomacromolecules*, 2013, **14**, 4483–4488.
37 D. Ma, J. Zhao, Y. Zhao, X. Hao, L. Li, L. Zhang, Y. Lu and C. Yu, *Colloids Surf. A*, 2012, **395**, 276–283.
38 S. Grabska-Zielinska and A. Sionkowska, *Materials*, 2021, **14**, 1510.
39 S. M. Sajadi, K. Kolo, M. Pirouei, S. A. Mahmud, J. A. Ali and S. M. Hamad, *RSC Adv.*, 2018, **8**, 35557–35568.
40 M. Z. Sarker, M. M. Rahman, H. Minami, T. Suzuki, M. K. Hossain and H. Ahmad, *Colloids Surf. A*, 2021, **617**, 126403.
41 A. Mondal, B. Adhikary and D. Mukherjee, *Colloids Surf. A*, 2015, **482**, 248–257.
42 A. Zainal Abidin, N. H. H. Abu Bakar, E. P. Ng and W. L. Tan, *J. Taibah Univ. Sci.*, 2017, **11**, 1070–1079.
43 M. Kgatle, K. Sikhwivhilu, G. Ndlovu and N. Moloto, *Catalysts*, 2021, **11**, 428.
44 M. Ismail, S. Gul, M. I. Khan, M. A. Khan, A. M. Asiri and S. B. Khan, *Green Process. Synth.*, 2019, **8**, 135–143.
45 M. A. Rabbi, M. M. Rahman, H. Minami, N. Yamashita, M. R. Habib and H. Ahmad, *Carbohydr. Polym.*, 2021, **251**, 117024.
46 M. Shahid, Z. H. Farooqi, R. Begum, M. Arif, M. Azam, A. Irfan and U. Farooq, *Z. Phys. Chem.*, 2022, **236**, 87–105.
47 S. Laouini, A. Bouafia and M. Tedjani, *Res. Sq.*, 2021, **18**, 1–26.
48 B. R. Ganapuram, M. Alle, R. Dadigala, A. Dasari, V. Maragoni and V. Guttena, *Int. Nano Lett.*, 2015, **5**, 215–222.
49 M. A. Salem, E. A. Bakr and H. G. El-Attar, *Spectrochim. Acta, Part A*, 2017, **173**, 188–195.
50 C. Umamaheswari, A. Lakshmanan and N. S. Nagarajan, *J. Photochem. Photobiol. B*, 2017, **170**, 125–133.
51 T. N. J. I. Edison, R. Atchudan, M. G. Sethuraman and Y. R. Lee, *J. Photochem. Photobiol. B*, 2016, **162**, 604–610.
52 A. Omidvar, B. Jaleh and M. Nasrollahzadeh, *J. Colloid Interface Sci.*, 2017, **490**, 11–21.
53 A. Murtaz, M. Uroos, M. Sultan, R. Muazzam and S. Naz, *RSC Adv.*, 2021, **11**, 26635–26644.
54 M. A. Rahman, P. Akter, M. R. Habib, M. A. Rahman, M. M. Mahiuddin, M. M. Rahman, M. S. Islam, M. A. J. Miah and H. Ahmad, *Bioconjugate Chem.*, 2025, **36**, 563–577.
55 M. A. Rahman, M. A. Rahman, M. A. Rabbi, M. Rana, M. R. Karim, M. A. J. Miah and H. Ahmad, *RSC Adv.*, 2024, **14**, 24447–24461.
56 X. Gu, Y. Yu, S. Zhong, Y. Zhang, H. Liu, J. Wang, Q. Li, R. Chen, Y. Zhao and Y. Liu, *Adv. Fiber Mater.*, 2025, **7**, 1529–1544.
57 A. F. Zatsepin, Y. A. Kuznetsova, D. A. Zatsepin, C. H. Wong, W. C. Law, C. Y. Tang and D. V. Boukhwalov, *J. Alloys Compd.*, 2023, **949**, 169815.

58 M. Gutiérrez and A. Henglein, *J. Phys. Chem.*, 1996, **100**, 7656–7661.
59 Y. Zhang, F. Li, K. Liu, T. Xu, T. Sun and L. Xu, *Nanoscale*, 2026, **18**, 3644–3650.
60 X. Liu, W. Li, N. Chen, X. Xing, C. Dong and Y. Wang, *RSC Adv.*, 2015, **5**, 34456–34465.
61 K. Naseem, Z. H. Farooqi, R. Begum and A. Irfan, *J. Cleaner Prod.*, 2018, **196**, 117–124.